Materials Advances

ROYAL SOCIETY OF CHEMISTRY

PAPER

View Article Online
View Journal | View Issue

Check for updates

Cite this: *Mater. Adv.*, 2024, 5, 6416

A disposal-MOX concept for plutonium disposition†

Max R. Cole,[a] Lewis R. Blackburn,[a] Latham T. Haigh,[a] Daniel J. Bailey,[a] Luke T. Townsend,[a] Kristina O. Kvashnina,[bc] Neil C. Hyatt[de] and Claire L. Corkhill *[d]

In case it is desirable to dispose of inventories of separated civil PuO_2 that have no further use, a suitable immobilisation matrix is required, prior to disposition in a geological disposal facility. Conversion of Pu into a mixed oxide (MOX)-type material with characteristics suitable for disposal has previously been suggested, but not yet demonstrated at laboratory or industrial scale. We here demonstrate the feasibility of different synthesis routes for simulant "disposal-MOX", using Th^{4+} as a Pu^{4+} surrogate and containing Gd^{3+} in a suitable quantity to ensure criticality control. Compositions of $(U_{(1-(x+y))}Th_xGd_y)O_{2-\delta}$, where x = 0.1, 0.2 and $x:y$ = 10 : 1 or 100 : 1, were synthesised by a solid state route mimicking the industrial MIMAS (MIcronized MASterblend) MOX fuel fabrication process, or through an oxalic wet co-precipitation method. Both synthesis routes gave a single phase fluorite structure upon heat-treatment at 1700 °C, with a grain size similar to $(Pu,U)O_2$ MOX fuel. The relative density of the sintered pellets was >90% but was highest in co-precipitated materials, with Th^{4+} and Gd^{3+} additions more homogenously distributed. Though no unincorporated ThO_2 or Gd_2O_3 was observed in any sample, Th and Gd-rich regions were more prevalent in materials produced through solid state synthesis, in accordance with MIMAS MOX fuel microstructures. The incorporation of Gd^{3+} within the fluorite lattice, which is favourable from a criticality control perspective in a Pu wasteform, was found to be charge balanced *via* the generation of oxygen vacancy defects, but not U^{5+}. These results demonstrate feasible synthesis routes for a disposal-MOX wasteform product *via* both solid state and wet co-precipitation fabrication routes.

Received 22nd April 2024,
Accepted 27th June 2024

DOI: 10.1039/d4ma00420e

rsc.li/materials-advances

Open Access Article. Published on 29 June 2024. Downloaded on 2/7/2026 5:36:32 PM.
This article is licensed under a Creative Commons Attribution 3.0 Unported Licence.

1. Introduction

The United Kingdom's inventory of separated Pu is forecast to reach 141 teHM (tonnes equivalent heavy metal). At present, the long-term management strategy for separated PuO_2, as outlined by the Nuclear Decommissioning Authority (NDA), stipulates that this material must be placed 'beyond reach'.[1] One option that could be considered for the whole inventory, should policy dictate, is immobilisation within a ceramic matrix, prior to disposition in a geological disposal facility.[2,3]

Disposal mixed oxide, herein referred to as 'disposal-MOX', was originally conceptualised by Macfarlane *et al.*,[4] and termed a 'low specification MOX' fuel product – a sintered solid solution of PuO_2 and UO_2 – without precise constraints on size as would be expected for reactor-grade MOX fuel. In this concept, then called "Plutonium Disposal – the Third Way", the low-specification MOX would be encapsulated within a vitrified borosilicate high level radioactive waste glass, which would serve as both a source of criticality control through the presence of boron, and also a proliferation barrier due to the high radiation field emanating from the glass.[5,6] A simpler and more effective criticality control could be provided by adding a neutron absorbing element to the PuO_2 and UO_2 blend, *e.g.*, Gd_2O_3 or HfO_2. Given that MOX fuel has been demonstrated at an industrial scale, this route could offer a potentially more appealing industrially-proven option for plutonium disposition when compared with technologically immature titanate ceramic materials fabricated by hot isostatic pressing, which are also being investigated as a potential route for plutonium disposition.[7–10] On the other hand, UK implementation of production scale MOX fuel manufacture, in the Sellafield MOX plant, proved problematic.

[a] *Immobilisation Science Laboratory, Department of Materials Science and Engineering, The University of Sheffield, UK*
[b] *Helmholtz-Zentrum Dresden-Rossendorf (HZDR), Institute of Resource Ecology, Germany*
[c] *The Rossendorf Beamline at ESRF – The European Synchrotron, CS40220, 38043 Grenoble Cedex 9, France*
[d] *School of Earth Sciences and the South West Nuclear Hub, The University of Bristol, UK. E-mail: c.corkhill@bristol.ac.uk*
[e] *School of Mechanical and Materials Engineering, Washington State University, Pullman, USA*

† Electronic supplementary information (ESI) available. See DOI: https://doi.org/10.1039/d4ma00420e

© 2024 The Author(s). Published by the Royal Society of Chemistry

Open Access Article. Published on 29 June 2024. Downloaded on 2/7/2026 5:36:32 PM. This article is licensed under a Creative Commons Attribution 3.0 Unported Licence.

Oxides of Pu and U adopt the cubic fluorite ($Fm\bar{3}m$) structure with comparable lattice dimensions (a = 5.470 Å and 5.398 Å for UO_2 and PuO_2, respectively). Furthermore, UO_2 and PuO_2 have similar densities, of 10.97 and 11.50 g cm^{-3}, respectively, and comparable melting points of 2827 °C and 2400 °C. As such, at the elevated temperatures used in wasteform processing (~1700 °C), there exists a complete solid solution between UO_2 and PuO_2 (in the form $U_{1-x}Pu_xO_2$), resulting in a relatively homogenous, single phase material.[11] When incorporated within a UO_2 solid solution, the neutron absorbing additive Gd_2O_3, also maintains the fluorite ($Fm\bar{3}m$) structure, up to 50 mol% Gd,[12] which should be significantly above the threshold required to mitigate criticality in management and disposal. Within the context of disposal in a geological facility, the adoption of the fluorite structure is advantageous since it exhibits high tolerance to radiation damage and can readily accommodate $He_{(g)}$ generated through alpha decay.[13,14] UO_2 and MOX fuels are also known to possess high aqueous durability under reducing conditions.[15,16] Moreover, the addition of Gd has been shown to reduce the rate of U release during dissolution.[17,18]

To demonstrate the feasibility of a disposal-MOX wasteform for Pu, we herein advance and demonstrate the concept of MacFarlane *et al.*[4] *via* investigation of disposal-MOX materials varying in composition and fabrication route. Oxide precursors were prepared through wet co-precipitation and conventional solid state mixed oxide synthesis routes to assess the influence of homogenisation on the final sintered disposal-MOX materials. The solid state fabrication route was based on the MIMAS (MIcronized MASterblend) process used to fabricate MOX fuel at the MELOX facility in France. This involves blending and milling UO_2 and PuO_2 powders into a 'master' blend before diluting with additional UO_2 to achieve the desired U : Pu ratio;[19] whereas, in the wet co-precipitation route, oxides were yielded from an oxalic precipitation of nitrate solutions, promoting higher homogeneity and phase purity. Samples were characterised to ascertain the influence of chemical composition and synthesis route on the final sintered microstructure, crystalline defects, distribution of the neutron absorber Gd and Pu surrogate, and oxidation state of U. As Pu is expected to maintain an oxidation state of +4 in disposal-MOX, Th, with its highly stable Th^{4+} oxidation state, was chosen as a surrogate for these demonstration trials.[20]

2. Experimental methodology and characterisation

2.1 Material synthesis

Four disposal-MOX compositions were produced, nominally: $U_{0.899}Th_{0.100}Gd_{0.001}O_{2-\delta}$, $U_{0.890}Th_{0.100}Gd_{0.010}O_{2-\delta}$, $U_{0.798}Th_{0.200}Gd_{0.002}O_{2-\delta}$ and $_{0.780}Th_{0.200}Gd_{0.020}O_{2-\delta}$. Th additions of 10 and 20 mol% represent realistic Pu content that could be incorporated within disposal-MOX. Similarly, the 100 : 1 ratio of Th : Gd reflects a reasoned estimate of the ratio of Pu : Gd required for criticality considerations in disposal environment scenarios. A greater 10 : 1 ratio was fabricated to investigate the effects of excessive Gd addition and to improve detection of Gd. The four compositions were produced using two distinct fabrication routes, wet co-precipitation, and solid-state mixed oxide synthesis, yielding a total of eight unique samples. Herein, samples will be referred to by their nominally targeted composition, though the reader is referred to Table 1 for measured compositions determined by inductively coupled plasma-optical emission spectroscopy (ICP-OES) following nitric acid digest and electron probe microanalysis (EPMA).

Wet co-precipitated samples were prepared through an oxalic precipitation route. Firstly, $UO_2(NO_3)_2{\cdot}6H_2O$ (British Drug House (BDH). B.D.H. Laboratory Chemicals Division, >98%), $Th(NO_3)_4{\cdot}6H_2O$ (British Drug House (BDH). B.D.H. Laboratory Chemicals Division, >98%) and $GdCl_3{\cdot}6H_2O$ (Sigma Aldrich, >99%) were dissolved in 1 M HCl to create solutions of known concentrations. Specific volumes of each solution, corresponding to the target chemical formula shown in Table 1, were mixed with the aid of a magnetic stirrer. The addition of 1 M oxalic acid promoted the instantaneous precipitation of mixed U, Th, and Gd oxalates. The oxalate precipitates were filtered and dried prior to calcination at temperatures ranging from 400 °C to 800 °C under a 5% H_2/95% N_2 atmosphere, yielding a fine oxide mixture. Approximately 200 mg of oxide powder calcined at 800 °C was pressed within a 6 mm stainless steel die to form loosely densified green bodies. No pore formers were used. Green bodies were placed onto a zirconia crucible and sintered at 1700 °C for 8 hours under a reducing 5% H_2/95% N_2 gas atmosphere, with a heating and cooling rate of 3 °C min^{-1}.

The solid state mixed oxide synthesis route was devised to resemble the MIMAS (MIcronized MASterblend) process

Table 1 Disposal-MOX compositions prepared by wet co-precipitation and solid-state mixed oxide synthesis. Compositions were measured using ICP-OES following total acid digest and by EPMA for selected samples. Quoted errors in total digest compositions were derived from the standard deviation of three repeat ICP-OES measurements. Errors in EPMA were derived from the standard deviation of five repeated quantitative spot measurements

Synthesis	Target formula	Measured (ICP digest)	Measured (EMPA)
Co-prec.	$U_{0.899}Th_{0.100}Gd_{0.001}O_{2-\delta}$	$U_{0.848(7)}Th_{0.146(7)}Gd_{0.006(2)}O_{2-\delta}$	$U_{0.825(3)}Th_{0.174(2)}Gd_{0.001(1)}O_{2-\delta}$
	$U_{0.890}Th_{0.100}Gd_{0.010}O_{2-\delta}$	$U_{0.835(5)}Th_{0.131(3)}Gd_{0.034(2)}O_{2-\delta}$	$U_{0.827(3)}Th_{0.165(2)}Gd_{0.008(1)}O_{2-\delta}$
	$U_{0.798}Th_{0.200}Gd_{0.002}O_{2-\delta}$	$U_{0.758(1)}Th_{0.234(9)}Gd_{0.008(0)}O_{2-\delta}$	—
	$U_{0.780}Th_{0.200}Gd_{0.020}O_{2-\delta}$	$U_{0.666(6)}Th_{0.266(4)}Gd_{0.069(2)}O_{2-\delta}$	$U_{0.655(3)}Th_{0.331(2)}Gd_{0.014(1)}O_{2-\delta}$
Solid state	$U_{0.899}Th_{0.100}Gd_{0.001}O_{2-\delta}$	$U_{0.889(3)}Th_{0.106(3)}Gd_{0.005(1)}O_{2-\delta}$	$U_{0.779(3)}Th_{0.221(3)}Gd_{0.000(1)}O_{2-\delta}$
	$U_{0.890}Th_{0.100}Gd_{0.010}O_{2-\delta}$	$U_{0.866(3)}Th_{0.105(2)}Gd_{0.029(2)}O_{2-\delta}$	$U_{0.863(3)}Th_{0.130(1)}Gd_{0.007(1)}O_{2-\delta}$
	$U_{0.798}Th_{0.200}Gd_{0.002}O_{2-\delta}$	$U_{0.801(4)}Th_{0.192(4)}Gd_{0.008(7)}O_{2-\delta}$	—
	$U_{0.780}Th_{0.200}Gd_{0.020}O_{2-\delta}$	$U_{0.759(4)}Th_{0.187(4)}Gd_{0.054(2)}O_{2-\delta}$	—

Open Access Article. Published on 29 June 2024. Downloaded on 2/7/2026 5:36:32 PM. This article is licensed under a Creative Commons Attribution 3.0 Unported Licence.

developed by BelgoNucleaire, by which the majority of commercial MOX fuels are fabricated.[21] The two-step MIMAS process involves creating a 'master' blend of UO_2 and PuO_2 that is subsequently diluted with UO_2 to achieve the desired U : Pu ratio in the final material. For this study, two master blends, corresponding with the two target Th : Gd ratios (1 : 100 and 1 : 10), were made by mixing appropriate masses of UO_2 (ABSCO Ltd, >98%), ThO_2 (decomposed from $Th(NO_3)_4{\cdot}6H_2O$, B.D.H. Laboratory Chemicals Division, >98%), and Gd_2O_3 (Sigma Aldrich, >99.9%) powders. Master blends were produced from constituent oxides *via* planetary milling, at 500 rpm for 1 h in propan-2-ol, to form a micronized blend that was subsequently sieved to achieve a particle size of less than 200 μm. This material was homogenised with additional UO_2 by roller milling for 24 h to yield the desired formulation as per the MIMAS flowsheet.[22] Milled, homogenised powders were pressed into green bodies and sintered as above.

2.2 Material characterisation

Thermal analysis was performed on the oxalate precipitates using a Netzsch TG 449 F3 Jupiter thermal analyser. Data was collected from simultaneous thermogravimetric (TG) and differential thermal (DT) analysis, in tandem with mass spectroscopy (MS), while oxalates were heated to temperatures of 1000 °C with a temperature ramp rate of 10 °C min^{-1}. Powder X-ray diffraction (XRD) analysis was performed on all precursors and sintered materials using a Bruker D2 Phaser fitted with a Lynxeye position sensitive detector. Data were acquired using a Cu-Kα source (λ = 1.5418 Å, Ni filter) in the range of $20^\circ \leq 2\theta \leq 80^\circ$, with a step size of 0.02°. Sintered powders were mixed with 10 wt% LaB_6 as an internal standard to support lattice parameter refinement performed by the Rietveld method.

Elemental concentrations in the sintered products were determined using two methods. Firstly, 20 mg of crushed sintered material was completely dissolved in 2 M HNO_3 at 90 °C, over 3 days, with the aid of constant mixing. The resulting solutions were diluted and analysed in triplicate using inductively coupled plasma-optical emission spectroscopy (ThermoFisher iCAPDuo6300) at the PLEIADES facility. External calibration was performed using single element standards (NIST traceable). Secondly, electron probe micro-analysis (EPMA) was undertaken using a JEOL JXA-8530F Plus Hyper Probe with an accelerating voltage of 15 kV and a probe current 100 nA. Compositions were measured using a minimum of five quantitative spot measurements, each at the centre of grains across the surface. Sintered pellets were polished to 1 μm and carbon coated to reduce surface charging effects. EPMA maps were collected for U, Th, Gd and O in stage mode, allowing the probe incident angle to remain constant during measurements to avoid errors associated with interaction volume changes.

Sintered pellet density was determined by the Archimedes method using a Mettler Toledo ME204 balance at room temperature using ethanol as the buoyancy medium. Ten repeat measurements were collected for each sample and the quoted error was calculated using the standard deviation of these measurements. Theoretical densities for each composition were calculated using the refined lattice parameters derived from XRD measurement.

Analysis of powder morphology and pellet microstructure was conducted using a Hitachi TM3030 SEM operating in backscattered electron (BSE) mode. EDS maps of powder samples were collected for a minimum of 10 minutes. Sintered pellets were polished to 1 μm and thermally etched at 1630 °C (90% of sintering temperature) to reveal the grain boundaries, allowing for grain size analysis through morphological segmentation using the MorphoLibJ plug-in suite[23] through the Fiji software package.[24] A minimum of 500 grains were analysed across several micrographs taken at random across the pellet surface to obtain a statistical average for each sample.

A Renishaw inVia microscope was used to conduct Raman spectroscopy on sintered pellets after polishing and annealing. Five sets of spectra, each of 15 acquisitions, were taken at the centre of grains with a 30 s acquisition time using a 514 nm laser set to 5 mW. These spectra were baseline subtracted, smoothed using the Savitsky–Golay approach and averaged. Deconvolution of Raman spectra was performed using Igor Pro software through the application of Gaussian peaks.

Uranium M_4-edge (3.725 keV) high energy resolution fluorescence detection X-ray absorption near edge spectroscopy (HERFD-XANES) was performed at the HZDR ROBL beamline of the European Synchrotron Radiation Facility.[25,26] The incident energy (3.725 keV) was selected with a Si(111) double-crystal monochromator and HERFD-XANES spectra were collected using five Si(220) crystal analysers at room temperature. Normalised U^{5+} content was determined using iterative transformation factor analysis (ITFA) and linear combination fitting (LCF) methods relative to well-characterised U standards. Linear combination fitting (LCF) was performed using Athena[27] and the proportion of U^{4+} and U^{5+} determined using the ITFA software package.[28]

3. Results and discussion

3.1 Characterisation of oxalate powders

Oxalate powders of each composition were found to crystallise in the monoclinic space groups $P2_1/c$, and $C2/c$. This is consistent with the precipitation, from solution, of mixed of U and Th oxalate, respectively[29] (Fig. 1a). The oxalates adopted a platelet morphology upon precipitation (Fig. 1b and Fig. S1, ESI†), with each platelet measuring ~5–10 μm in all samples. EDS mapping indicated that each platelet contained a mixture of U, Th and Gd (Fig. 1b), as a homogeneous single oxalate phase, or an intimate mixture of separate U, Th and Gd oxalates.

Complete decomposition to the base oxides occurred by ~600 °C as shown by thermogravimetric (TG) and differential thermal analysis (DA) (Fig. 2a). Two major mass losses at temperatures of <320 °C (T_1 and T_2), corresponding to water loss as the oxalates were dehydrated (Fig. 2a) were observed, and a mass loss at 320 °C (T_3) was attributed to CO_2 evolution

 © 2024 The Author(s). Published by the Royal Society of Chemistry

Open Access Article. Published on 29 June 2024. Downloaded on 2/7/2026 5:36:32 PM.
This article is licensed under a Creative Commons Attribution 3.0 Unported Licence.

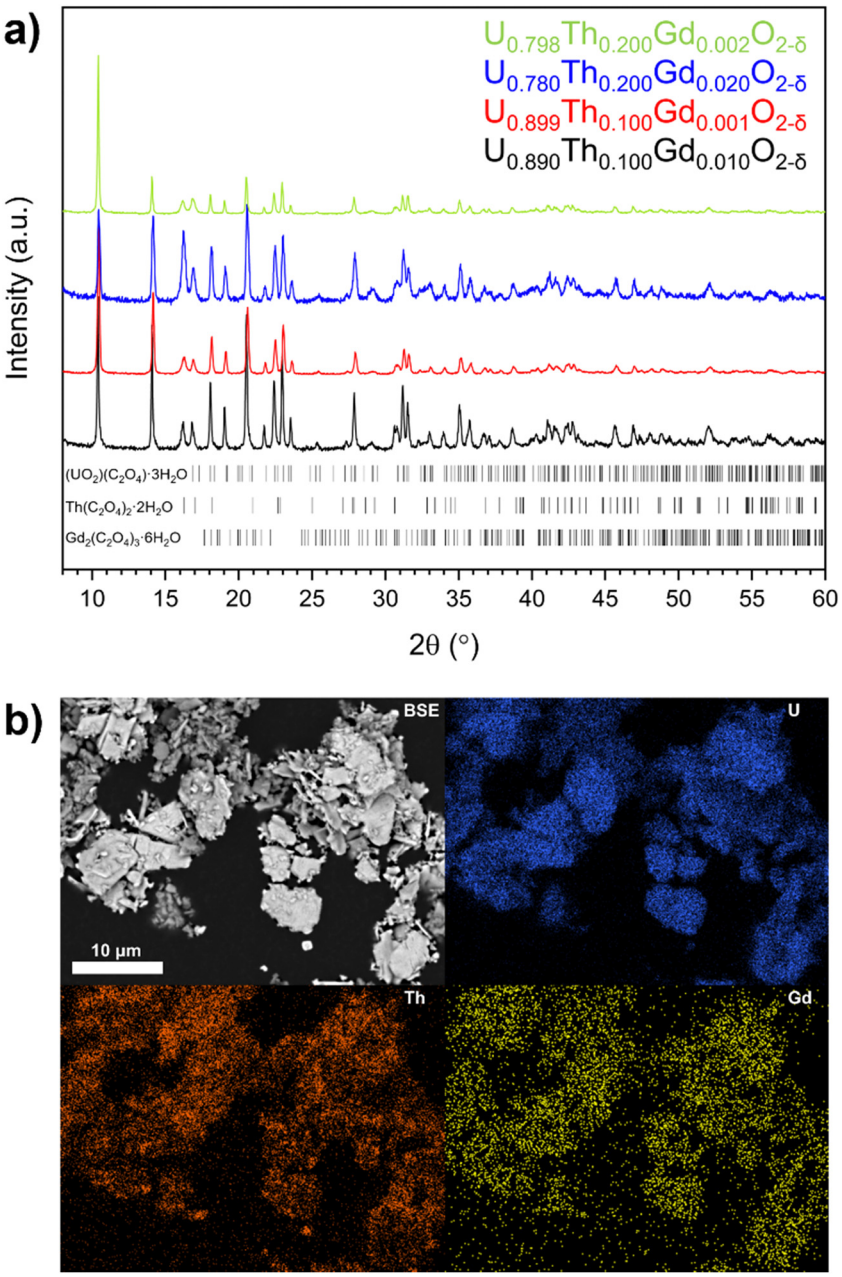

Fig. 1 (a) XRD data for synthesised oxalate powders, highlighting reflections indexed to oxalates of U (ICSD card no. #172778), Th (ICSD card no. #248038) and Gd (ICSD card no. #121695). (b) BSE micrograph and EDS element distribution maps of the oxalate precursor for the nominal $U_{0.798}Th_{0.200}Gd_{0.002}O_{2-\delta}$ composition.

during decomposition of the oxalate (Fig. S2, ESI†). Each of these phenomena exhibited additional features; for example, at T_1 and T_2, there are two features, and T_3 exhibits three (Fig. 2a). This supports the presence of separate oxalates of U, Th and Gd, although it does not rule out the presence of at least a portion of mixed oxalate. No further mass losses were measured upon heating beyond 600 °C. Two endothermic transformations were assigned to water loss between 90 °C and 320 °C, while exothermic reactions corresponding to CO_2 and CO evolution occurred between 330 °C and 420 °C, in agreement with the TG data.

Oxide powders produced by the thermal decomposition of the nominal $U_{0.798}Th_{0.200}Gd_{0.002}O_{2-\delta}$ material at 400 °C, 800 °C and 1000 °C were analysed by XRD (Fig. 2b). The peak broadening observed in the oxide calcined at 400 °C, when compared with the materials calcined at higher temperature, indicates a significantly smaller crystallite size. Reflections relating to oxalate were not observed in either the 800 °C or 1000 °C calcined oxides, suggesting successful decomposition to oxide at these temperatures, in accordance with corresponding TG data on the same material. Gd_2O_3 was not observed in any of the calcined powders, suggesting complete incorporation

© 2024 The Author(s). Published by the Royal Society of Chemistry

Open Access Article. Published on 29 June 2024. Downloaded on 2/7/2026 5:36:32 PM.
This article is licensed under a Creative Commons Attribution 3.0 Unported Licence.

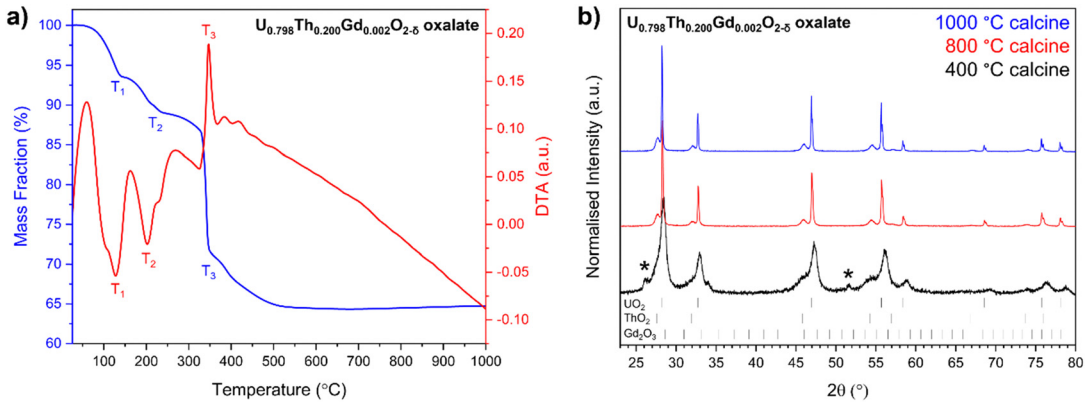

Fig. 2 (a) Thermal analysis of the oxalate powder prepared to form $U_{0.798}Th_{0.200}Gd_{0.002}O_{2-\delta}$ co-precipitated pellets and; (b) XRD data collected on $U_{0.798}Th_{0.200}Gd_{0.002}O_{2-\delta}$ oxide powders decomposed from oxalates at 400 °C, 800 °C and 1000 °C. Two sets of fluorite peaks are indexed to UO_2 (ICSD card no. #160814) and ThO_2 (ICSD card no. #253564). Additional peaks denoted with '*' in the 400 °C trace correspond with residual oxalate content, indicating incomplete decomposition. Cubic C-type Gd_2O_3 (ICSD card no. #94892) peaks were absent in all traces.

within a solid solution with at least one of the other constituents, or that it was present at concentrations below the detection limit of the XRD. The optimum calcination temperature for all oxalates was selected to be 800 °C, as this was evidenced to fully decompose each compound into oxides. The decomposition of the oxalate into distinct ThO_2 and UO_2 phases was observed for all targeted compositions, supporting the hypothesis that more than one oxalate was formed during the precipitation from solution (Fig. S3, ESI†).

3.2 Characterisation of sintered disposal-MOX

3.2.1 Disposal-MOX average composition. Compositional analysis of sintered disposal-MOX materials derived from total acid digest revealed that all four co-precipitated samples contained excess quantities of Th and Gd relative to the target composition (Table 1). This deviation from nominal stoichiometry is likely due to incomplete conversion of $UO_2(NO_3)_2$ to $UO_2C_2O_4$ during the precipitation reaction, as indicated by the yellow colour of the supernatant solution after precipitation (*i.e.*, containing residual uranyl nitrate). The pH of the oxalic solution was pH < 1, which is somewhat lower than ideal for the precipitation of uranyl oxalate,[30] explaining the incomplete reaction. Since an excess of oxalic acid was added, this behaviour is not attributed to the formation of separate oxalates of U, Th and Gd. Materials prepared by the solid state route were close to the nominal composition; for example, the Th content was within 10% of the desired stoichiometry relative to U in all solid state samples. The Gd additions were further from the desired stoichiometry, which can be attributed to precision when targeting small batch sizes of 5 g; for example, to yield a Th : Gd ratio of 100 : 1 at a 5 g scale requires a Gd_2O_3 mass of 0.0039 g. Quantitative EPMA point spectra collected on sintered pellets provided comparison with the bulk analysis provided by the total acid digest method (Table 1). Both methods were in good agreement with one another, despite differences induced by the nature of the measurements (EPMA samples individual points in a heterogenous matrix, while ICP-MS measures the composition of a completely dissolved material), and confirmed that materials prepared by the solid state route achieved compositions closer to those targeted than the co-precipitated samples, and that Th and Gd concentrations were in excess of desired stoichiometries in all co-precipitated samples.

3.2.2 Crystal structure and chemistry of disposal-MOX. Following sintering at 1700 °C under 5% H_2/N_2, each composition, regardless of fabrication route, formed a single phase fluorite compound as exemplified by a single set of cubic reflections characteristic of the $Fm\bar{3}m$ space group (Fig. 3). The lack of additional ThO_2 or Gd_2O_3 reflections indicated complete incorporation of both Th^{4+} and Gd^{3+} cations into solid solution within the UO_2 matrix.

Corresponding Rietveld analysis (Table 2) revealed that Th^{4+} substitution, irrespective of synthesis route, resulted in an increase in the unit cell parameter a (Å) relative to the host UO_2 matrix, consistent with the relative size of Th^{4+} and U^{4+} in 8-fold coordination (1.19 Å and 1.14 Å, respectively). Whilst Gd^{3+} is slightly larger (1.193 Å), it is known to have the opposite effect on the lattice parameter of UO_2 due to the lattice contraction resulting from the generation of oxygen vacancies (V_O) or U^{5+} (radius 0.89 Å) in the charge compensation required for the incorporation of a trivalent species on a tetravalent site.[31–33] The addition of Gd^{3+} was shown to result in a decrease in the lattice parameter in sintered materials, particularly for the materials prepared by the solid state route.

In accordance with the XRD data, lattice disorder relative to pure UO_2 was indicated by a broadening and shift in the Raman in T_{2g} mode at 445 cm^{-1} (Fig. 4), which is characteristic of the fluorite structure, to higher wavenumbers.[31,34] The magnitude of the shift varied linearly with total Th^{4+} and Gd^{3+} additions (Table S1, ESI†). The Raman spectra exhibited a broad set of overlapping bands at 575 cm^{-1}, referred to as the defect region, which can be deconvoluted to reveal individual contributions from three distinct defect bands: U_1, U_2 and U_3. The U_1 band, which typically occurs around 540 cm^{-1}, results from lattice distortion due to V_O.[31–35] The intensity of the U_1 band, measured by its full width half maximum (FWHM), was found to

© 2024 The Author(s). Published by the Royal Society of Chemistry

Open Access Article. Published on 29 June 2024. Downloaded on 2/7/2026 5:36:32 PM.
This article is licensed under a Creative Commons Attribution 3.0 Unported Licence.

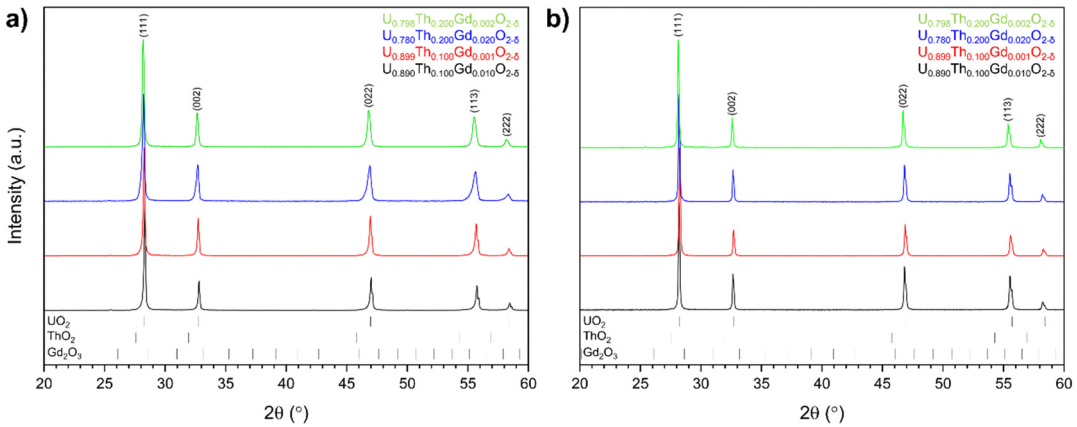

Fig. 3 X-ray diffraction analysis for disposal-MOX materials produced by (a) solid state and; (b) co-precipitation routes.

Table 2 Lattice parameters for disposal-MOX materials prepared using co-precipitation and solid state routes. Listed compositions are bulk compositions derived from total acid digest. R_{wp} (weighted profile R-factor and χ^2 are statistical parameters that indicate the goodness of fit)

Synthesis route	Composition	a (Å)	R_{wp} (%)	χ^2
Co-prec.	$U_{0.848(7)}Th_{0.146(7)}Gd_{0.006(2)}O_{2-\delta}$	5.49134(8)	10.495	1.566
Co-prec.	$U_{0.835(5)}Th_{0.131(3)}Gd_{0.034(2)}O_{2-\delta}$	5.48806(5)	10.000	1.724
Co-prec.	$U_{0.758(1)}Th_{0.234(9)}Gd_{0.008(0)}O_{2-\delta}$	5.50454(6)	11.331	2.085
Co-prec.	$U_{0.666(6)}Th_{0.266(4)}Gd_{0.069(2)}O_{2-\delta}$	5.50871(5)	9.832	1.723
Solid state	$U_{0.889(3)}Th_{0.106(3)}Gd_{0.005(1)}O_{2-\delta}$	5.48019(1)	14.465	2.343
Solid state	$U_{0.866(3)}Th_{0.105(2)}Gd_{0.029(2)}O_{2-\delta}$	5.47731(1)	16.764	2.609
Solid state	$U_{0.801(4)}Th_{0.192(4)}Gd_{0.008(7)}O_{2-\delta}$	5.49585(1)	11.284	1.721
Solid state	$U_{0.759(4)}Th_{0.187(4)}Gd_{0.054(2)}O_{2-\delta}$	5.49042(2)	16.086	2.576

increase with increasing Gd^{3+} content (Fig. S5, ESI†), suggesting that Gd^{3+} incorporation into the UO_2 lattice was charge compensated *via* V_O generation regardless of compositions or fabrication route. The U_2 band, also known as the resonant first-order longitudinal optical (1LO) mode, is activated as the perfect fluorite symmetry is broken. This band was the most intense in samples with greatest Th^{4+} and Gd^{3+} content, a result of increased disorder due to incorporation of these differently sized cations within the UO_2 lattice, and from V_O generation.[34] The U_3 band can be assigned to cuboctahedral symmetry, which results from oxygen interstitials forming a hyper-stoichiometric U_4O_9 structure. The low intensity of this band in all spectra confirms the absence of highly oxidised clusters. The full suite of Raman data for all samples is given in Fig. S4 (ESI†).

To determine whether a portion of the U in disposal-MOX was oxidised to U^{5+} to charge compensate for the incorporation of Gd^{3+}, U M_4-edge HERFD-XANES spectra were collected on

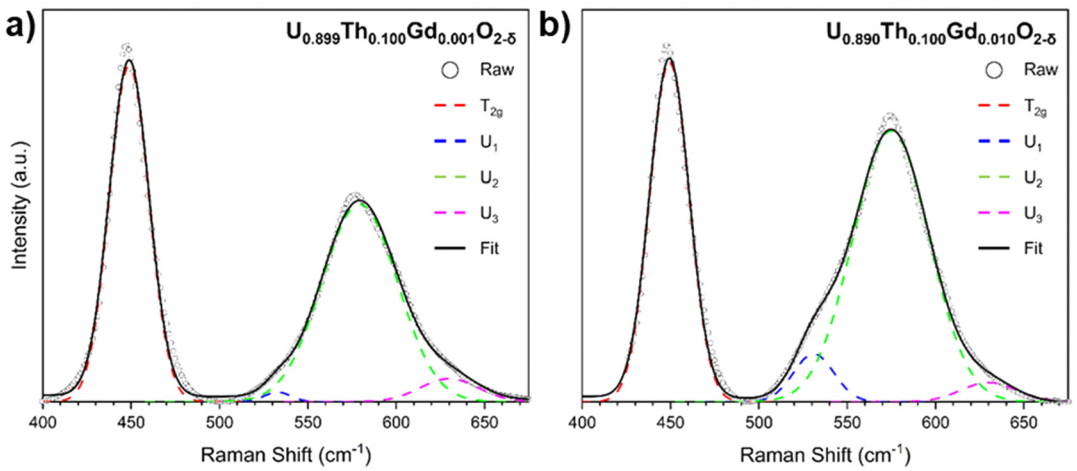

Fig. 4 Deconvoluted Raman spectra for coprecipitated materials targeting nominal compositions (a) $U_{0.899}Th_{0.100}Gd_{0.001}O_{2-\delta}$ and (b) $U_{0.890}Th_{0.100}Gd_{0.010}O_{2-\delta}$.

Open Access Article. Published on 29 June 2024. Downloaded on 2/7/2026 5:36:32 PM.
This article is licensed under a Creative Commons Attribution 3.0 Unported Licence.

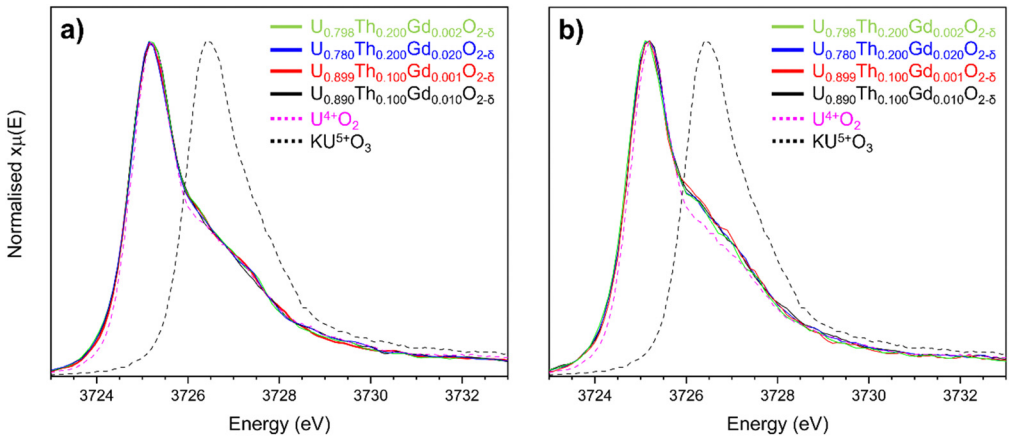

Fig. 5 Comparison of U M_4-edge HERFD-XANES spectra collected on (a) solid state and (b) co-precipitated disposal-MOX samples alongside representative U^{4+} and U^{5+} reference compounds.

sintered pellets of each composition. The obtained spectra were normalised and fit using linear combination fitting (LCF) and verified with iterative transformation factor analysis (ITFA), as presented in Fig. 5. When comparing the spectral features to the known $KU^{5+}O_3$ reference compound, it was apparent that no U^{5+} was present in any of the targeted compositions (Fig. 5a).[36,37] For the samples prepared by the co-precipitated route, a shoulder was present on the high energy side of the peak representative of U^{4+}, which was not present for the solid state materials; this could be attributed to disorder within the UO_2 lattice,[38,39] in agreement with the XRD and Raman spectroscopy data. These results strongly indicate that V_O generation, not oxidation to U^{5+}, is the dominant charge compensation mechanism for all the obtained disposal-MOX samples.

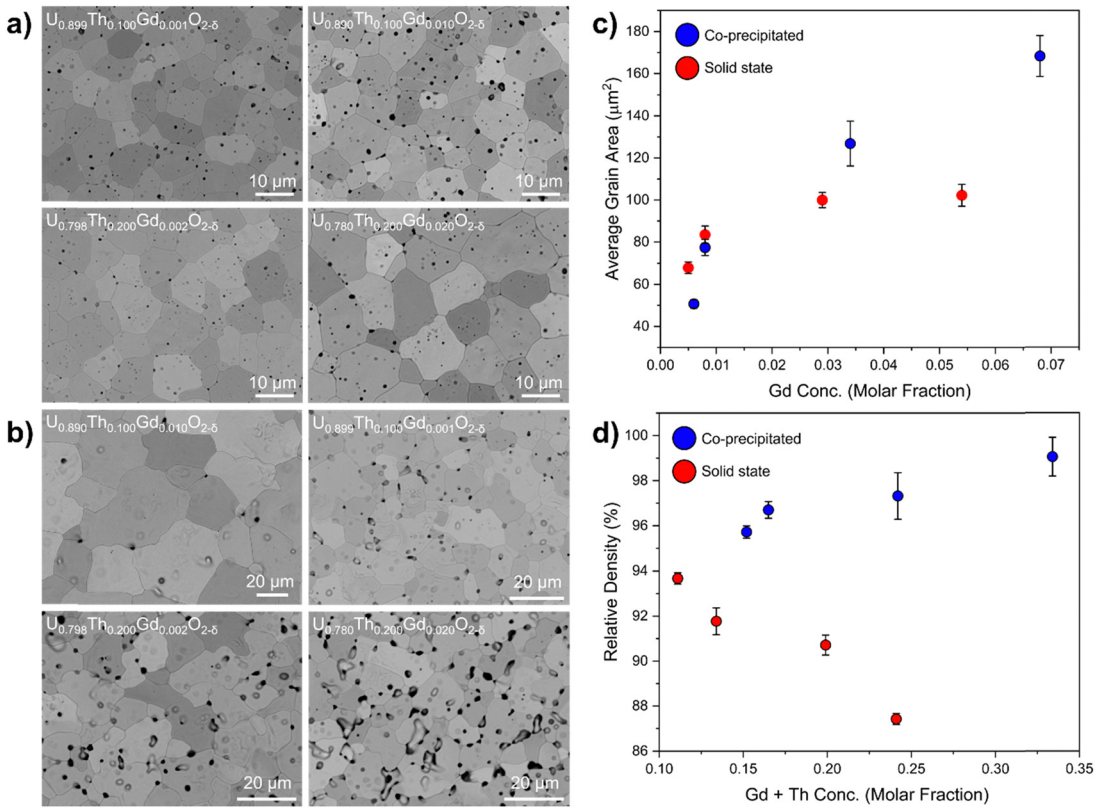

Fig. 6 Microstructure and density analysis of disposal-MOX materials. Showing (a) BSE images of co-precipitated pellets; (b) BSE images of pellets prepared by the solid state route; (c) plot of average grain size as a function of the molar fraction of Gd; and (d) the relative density as a function of the molar fraction of Th and Gd. Relative density was calculated by dividing the measured density by the theoretical density. Theoretical density was calculated using refined lattice parameters and compositions measured by ICP-OES.

© 2024 The Author(s). Published by the Royal Society of Chemistry

Open Access Article. Published on 29 June 2024. Downloaded on 2/7/2026 5:36:32 PM.
This article is licensed under a Creative Commons Attribution 3.0 Unported Licence.

3.2.3 Microstructure analysis of disposal-MOX. The sintered disposal-MOX materials were dense with a well-equiaxed grain structure and exhibited a microstructure similar to that observed for UO_2, ThO_2 and $(U,Pu)O_2$ (Fig. 6a and b); however, some intragranular porosity was observed.[40–42] Similar observations of intragranular porosity in $(U,Ce)O_2$ were made by Harrison *et al.*,[40] who proposed oxygen release due to V_O formation as the potential cause. In co-precipitated samples, continued CO/CO_2 evolution during sintering may also have contributed to this porosity. Although the TG-MS analysis showed no further gas evolution after temperatures exceeded 600 °C, it is possible that residual carbon remained following calcination at 800 °C. For example, Horlait *et al.* reported at least 0.25 wt% residual carbon in Am-doped UO_2 oxides calcined from oxalates at 750 °C.[43]

When compared with co-precipitated materials, the materials prepared by the solid state route showed signs of poor sinterability, with an unusual morphology, variance in grain size and more extensive intergranular porosity. Lower rates of diffusion during the sintering of the solid state samples evidenced poor homogenisation and lower reactive surface area of the milled oxides compared to those produced *via* wet co-precipitation. It is possible that the Gd is already dissolved in UO_2 in materials prepared by the co-precipitation route, enhancing diffusion relative to the solid state route materials, in which Gd is not as intimately mixed. In both co-precipitated and solid state samples, the grain size was observed to increase with increasing Gd concentration (Fig. 6c). The relative density of the co-precipitated samples increased gradually with increasing Th and Gd content, correlating well with the measured

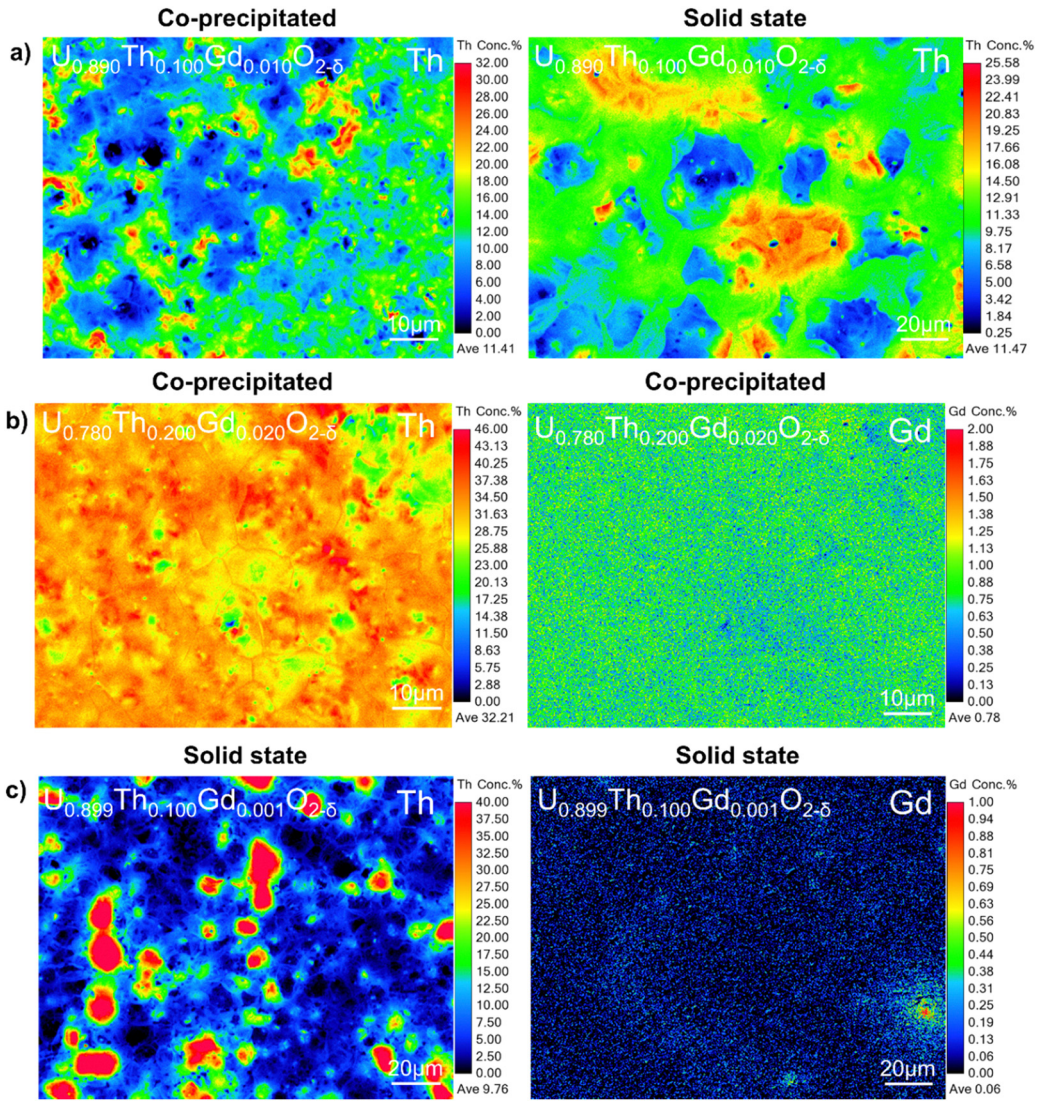

Fig. 7 Elemental distribution of Th^{4+} and Gd^{3+} in disposal-MOX samples. Showing EMPA maps of (a) comparable compositions prepared by co-precipitation and solid state routes (note the different scale); (b) co-precipitated pellets revealing homogeneity of Th and Gd distribution; and (c) solid state pellets revealing lack of correlation between areas of elevated Th^{4+} and Gd^{3+} content.

© 2024 The Author(s). Published by the Royal Society of Chemistry

Open Access Article. Published on 29 June 2024. Downloaded on 2/7/2026 5:36:32 PM. This article is licensed under a Creative Commons Attribution 3.0 Unported Licence.

grain size increase; however, in the pellets prepared by the solid state route, the opposite trend was observed. This is likely correlated with the increased intergranular porosity in compositions containing a greater amount of Th^{4+}.

3.2.4 Distribution of Th^{4+} and Gd^{3+} in disposal-MOX. High resolution compositional mapping by EPMA (Fig. 7 and Fig. S5–S9, ESI†) revealed greater compositional heterogeneity in the disposal-MOX pellets fabricated *via* the solid state route, when compared to those prepared by wet co-precipitation (Fig. 7a). Large ($\sim$20 μm) regions enriched with Th^{4+} were readily observed in the solid state route samples (Fig. 7a and c), whereas Th was far more homogenously distributed in the co-precipitated materials (Fig. 7a). The measured Th^{4+} content in the solid state route materials was greatest ($\sim$80 at%) at the centre of the Th-rich agglomerates, with the surrounding rim enriched to a lesser extent. This gradient of Th^{4+} concentration suggests incomplete diffusion of ThO_2 powders into the UO_2 matrix during sintering as a result of poorer homogenisation and large particle size, potentially due to insufficient milling. Consequently, large areas of the materials prepared by the solid state route were entirely free of Th (Fig. 7c). This effectively simulates the microstructure of the MIMAS preparation route for fuel grade $(U,Pu)O_2$ MOX fuel, which exhibits distinct islands of PuO_2;[44] although additional milling of the solid state samples may yield an even more representative microstructure.

Although the co-precipitated materials were more homogeneous, they also exhibited areas that contained both Th and Gd, at concentrations of approximately 30–40 at% and $>$1 at%, respectively (Fig. 7a and b). Regions of elevated Th^{4+} did not typically correlate with Gd-rich regions in the solid state samples (Fig. 7c), confirming that this behaviour was dependent on fabrication route. This may be important when considering the necessity of Gd, a neutron absorber, to be in close proximity to Pu to provide a robust control on criticality.

4. Conclusions

Two synthesis routes for the fabrication of a conceptual disposal-MOX wasteform for the immobilisation of separated Pu inventories were demonstrated. Single phase cubic fluorite materials were obtained for all compositions produced using both oxalic co-precipitation and solid state synthesis routes – the latter mimicking the MIMAS MOX fuel synthesis route – as confirmed by XRD. The incorporation of Th^{4+}, as a structural surrogate for Pu^{4+} in UO_2, was evidenced through an expansion of the fluorite lattice, whereas Gd^{3+} additions contracted the lattice due to V_O generation in a charge compensation mechanism, evidenced by deconvolution of Raman spectroscopy. Materials prepared *via* the solid state route successfully reproduced the MIMAS MOX-fuel microstructure, although further milling optimisation studies are warranted. The application of U M_4 HERFD-XANES indicated that U^{5+} was not stabilised in appreciable concentrations in materials produced by either synthesis route. The main difference between the two synthesis routes was not in the chemistry, but in the distribution of Th^{4+} and Gd^{3+} as well as the overall microstructure, which was more heterogeneous in materials prepared by the solid state route method. Although single phase disposal-MOX could feasibly be produced by either synthesis route, the adaptability of the MIMAS process to produce $(U,Pu,Gd)O_2$ pellets at an industrial scale is clearly more compatible with a PuO_2 feedstock. These data set a benchmark for further disposal-MOX studies, in an effort to underpin its suitability for geological disposal, including industrial fabrication, aqueous durability, radiation damage tolerance and mechanical properties.

Data availability

The data that support the findings of this study are available from the corresponding author, upon reasonable request.

Conflicts of interest

There are no conflicts to declare.

Acknowledgements

This research utilised the National Nuclear User Facilities HADES[45] and PLEIADES, established with financial support from the UK Engineering and Physical Science Research Council (EPSRC) and BEIS (EP/T011424/1, EP/V035215/1). CLC is grateful to EPSRC for the award of an ECR Fellowship (EP/N017374/1) and for funding under the TRANSCEND consortium (EP/S01019X/1). LRB wishes to thank the Royal Academy of Engineering for funding through the Research Fellowship scheme. We gratefully acknowledge Stuart Creasey-Gray for assistance in collecting the EPMA data. We acknowledge the European Synchrotron Radiation Facility for provision of synchrotron radiation facilities (under proposal number MA-4821) and we would like to thank Tatiana Poliakova, Anastasiia Smirnova and Jurij Galanzew for assistance in using the Rossendorf beamline (ROBL, BM20) remotely during the pandemic. Sarah Pepper, Ritesh Mohun, Josh Radford and Hannah Smith are gratefully acknowledged for their assistance with data collection, and we wish to thank Paul Cook and Paul Heath from, respectively, the Nuclear Decommissioning Authority and Nuclear Waste Services, for insightful discussions regarding the data and the context of the work.

References

1 Nuclear Decommissioning Authority, ''Progress on Plutonium Consolidation, Storage and Disposition,'' 2019.
2 N. C. Hyatt, *Energy Policy*, 2017, **101**, 303–309.
3 N. C. Hyatt, *npj Mater. Degrad.*, 2020, **4**, 28.
4 A. M. MacFarlane, F. von Hippel, J. Kang and R. Nelson, *Bull. At. Sci.*, 2001, **57**, 53–57.
5 J. Kang, F. N. von Hippel, A. MacFarlane and R. Nelson, *Sci. Global Security*, 2002, **10**(2), 85–101.
6 A. M. Macfarlane, *Prog. Nucl. Energy*, 2007, **49**(8), 644–650.

© 2024 The Author(s). Published by the Royal Society of Chemistry

Open Access Article. Published on 29 June 2024. Downloaded on 2/7/2026 5:36:32 PM. This article is licensed under a Creative Commons Attribution 3.0 Unported Licence.

7 G. Lumpkin, *Elements*, 2006, **2**, 365–372.
8 S. M. Thornber, M. C. Stennett, E. R. Vance, D. T. Chavara, I. Watson, M. Jovanovic, J. Davis, D. Gregg and N. C. Hyatt, *MRS Adv.*, 2018, **3**, 1065–1071.
9 D. J. Gregg, R. Farzana, P. Dayal, R. Holmes and G. Triani, *J. Am. Ceram. Soc.*, 2020, **103**, 5424–5441.
10 L. R. Blackburn and N. C. Hyatt, *Enc. Nucl. Energy*, 2021, pp. 650–662.
11 R. Böhler, M. J. Welland, D. Prieur, P. Cakir, T. Vitova, T. Preussmann, I. Pidchenko, C. Hennig, C. Gueneau, R. J. M. Konings and D. Manara, *J. Nucl. Mater.*, 2014, **448**, 330–339.
12 M. Durazzo, F. B. V. Oliveira, E. F. Urano De Carvalho and H. G. Riella, *J. Nucl. Mater.*, 2010, **400**, 183–188.
13 F. Garrido, S. Moll, G. Sattonnay, L. Thomé and L. Vincent, *Nucl. Instrum. Methods Phys. Res., Sect. B*, 2009, **267**, 1451–1455.
14 T. Wiss, J.-P. Hiernaut, D. Roudil, J.-Y. Colle, E. Maugeri, Z. Talip, A. Janssen, V. Rondinella, R. J. M. Konings, H.-J. Matzke and W. J. Weber, *J. Nucl. Mater.*, 2014, **451**, 198–206.
15 D. W. Shoesmith, *J. Nucl. Mater.*, 2000, **282**, 1–31.
16 A. Leenaers, L. Sannen, S. Van den Berghe and M. Verwerft, *J. Nucl. Mater.*, 2003, **317**, 226–233.
17 A. Casella, B. Hanson and W. Miller, *J. Nucl. Mater.*, 2016, **476**, 45–55.
18 M. Razdan and D. W. Shoesmith, *J. Electrochem. Soc.*, 2014, **161**, H105–H113.
19 Z. Talip, S. Peuget, M. Magnin, M. Tribet, C. Valot, R. Vauchy and C. Jegou, *J. Nucl. Mater.*, 2018, **499**, 88–97.
20 P. A. Bingham, R. J. Hand, M. C. Stennett, N. C. Hyatt and M. T. Harrison, *Mater. Res. Soc. Symp. Proc.*, 2008, **1107**, 421–428.
21 H. Bariot, J. Van Vliet, G. Chiarelli, J. Edwards, S. H. Nagai and F. Reshnetnikov, International Atomic Energy Agency, 2000, IAEA-SM-358/VII link.
22 D. Warin, M. Bauer, M. Seiss and R. Lorenzelli, International Atomic Energy Agency, 1997, IAEA-TECDOC-941 link.
23 D. Legland, I. Arganda-Carreras and P. Andrey, *Bioinformatics*, 2016, **32**, 3532–3534.
24 J. Schindelin, *et al.*, *Nat. Methods*, 2012, **9**, 676–682.
25 A. C. Scheinost, J. Claussner, J. Exner, M. Feig, S. Findeisne, C. Hennig, K. O. Kvashnina, D. Naudet, D. Prieur, A. Rossberg, M. Schmidt, C. Qiu, P. Colomp, C. Cohen, E. Dettona, V. Dyadkin and T. Stumpf, *J. Synchrotron Radiat.*, 2021, **28**, 333–349.
26 K. O. Kvashnina and A. C. Scheinost, *J. Synchrotron Radiat.*, 2016, **23**, 836–841.
27 B. Ravel and M. Newville, *J. Synchrotron Radiat.*, 2005, **12**, 537–541.
28 A. Rossberg, K. U. Ulrich, S. Weiss, S. Tsushima, T. Hiemstra and A. C. Scheinost, *Environ. Sci. Technol.*, 2009, **43**, 1400–1406.
29 V. Tyrpekl, J. F. Vigier, D. Manara, T. Wiss, O. Dieste Blanco and J. Somers, *J. Nucl. Mater.*, 2015, **460**, 200–208.
30 Y. J. Shin, I. S. Kim, W. K. Lee, H. S. Shin and S. G. Ro, *J. Radioanal. Nucl. Chem.*, 1996, **209**, 217–223.
31 S. Karcher, R. Mohun, T. Olds, M. Weber, K. Kriegsman, X. Zhao, X. Guo, C. Corkhill, D. Field and J. McCloy, *J. Raman Spectrosc.*, 2022, **53**, 988–1002.
32 H. Smith, L. T. Townsend, R. Mohun, T. Cordara, M. C. Stennett, J. F. W. Mosselmans, K. O. Kvashnina and C. L. Corkhill, *Chem. Commun.*, 2022, **5**, 163.
33 H. Smith, L. T. Townsend, R. Mohun, J. F. W. Mosselmans, K. Kvashnina, N. C. Hyatt and C. L. Corkhill, *Sci. Rep.*, 2024, **14**, 1656.
34 G. Guimbretière, L. Desgranges, A. Canizares, G. Carlot, R. Caraballo, C. Jegou, F. Duavl, N. Raimbous, M. R. Ammar and P. Simon, *Appl. Phys. Lett.*, 2012, **100**, 251914.
35 J. Lee, J. Kim., Y.-S. Youn, N. Liu, J.-G. Kim, Y.-K. Ha, D. W. Shoesmith and J.-Y. Sun, *J. Nucl. Mater.*, 2017, **486**, 216–221.
36 K. O. Kvashnina, S. M. Butorin, P. Martin and P. Glatzel, *Phys. Rev. Lett.*, 2013, **111**, 253002.
37 K. O. Kvashnina and S. M. Butorin, *Chem. Commun.*, 2022, **58**, 327.
38 D. Prieur, L. Martel, J.-F. Vigier, A. C. Scheinost, K. O. Kvashnina, J. Somers and P. M. Martin, *Inorg. Chem.*, 2018, **57**, 1535–1544.
39 E. Gerber, A. Y. Romanchuk, S. Weiss, S. Bauters, B. Schacherl, T. Vitova, R. Hubner, S. S. A. Azzam, D. Detollenaere, D. Banerjee, S. M. Butorin, S. N. Kalmykov and K. O. Kvashnina, *Inorg. Chem. Front.*, 2021, **8**, 1102–1110.
40 R. W. Harrison, J. Morgan, J. Buckley, T. Abram, D. T. Goddard and N. J. Barron, *J. Nucl. Mater.*, 2021, **557**, 153302.
41 Y. Cherkaski, N. Clavier, L. Brissonneau, R. Podor and N. Dacheux, *J. Eur. Ceram. Soc.*, 2017, **37**, 3381–3391.
42 N. Hingant, N. Clavier, N. Dacheux, S. Hubert, N. Barre, R. Podor and L. Aranda, *Powder Technol.*, 2011, **208**, 454–460.
43 D. Horlait, F. Lebreton, A. Gauthe, M. Caisso, B. Arab-Chapelet, S. Picart and T. Delahaye, *J. Nucl. Mater.*, 2014, **444**, 181–185.
44 J. Noirot, L. Desgranges and J. Lamontagne, *J. Nucl. Mater.*, 2008, **372**, 318–339.
45 N. C. Hyatt, C. L. Corkhill, M. C. Stennett, R. J. Hand, L. J. Gardner and C. L. Thorpe, *IOP Conf. Ser.: Mater. Sci. Eng.*, 2020, **818**, 012022.

© 2024 The Author(s). Published by the Royal Society of Chemistry